M.O. VASYLYEV[1,*], B.M. MORDYUK[1,**], and S.M. VOLOSHKO[2]

[1] G.V. Kurdyumov Institute for Metal Physics of the N.A.S. of Ukraine,
36 Academician Vernadsky Blvd., UA-03142 Kyiv, Ukraine
[2] National Technical University of Ukraine
'Igor Sikorsky Kyiv Polytechnic Institute',
37 Beresteiskyi Prosp., UA-03056 Kyiv, Ukraine

* vasil@imp.kiev.ua, vasil1934@ukr.net; ** mordyuk@imp.kiev.ua

SURFACE POST-PROCESSING OF INCONEL 718 ALLOY FABRICATED BY ADDITIVE MANUFACTURING: SELECTIVE LASER MELTING

The review analyses Inconel 718 (IN718) alloy, which is the nickel-based superalloy and has great application in industries due to its superior mechanical properties even at elevated temperatures by means of the solid-solution strengthening and precipitation strengthening. However, because of the tool over-wear, poor part surface integrity, high hardness and low thermal-conductivity properties, it is difficult to manufacture finished products with using conventional machining methods. It is especially urgent for the products of complex designs. In this regard, justification is given for the widespread use of modern additive manufacturing (AM) for the fabrication of the products from IN718. The most popular is AM based on the selective laser melting (SLM) technique, which can fabricate complex geometries with superior material properties. At the same time, the metal parts fabricated by SLM suffer from excessive residual porosity, residual tensile stress in the near-surface layer, and the formation of a relatively rough surface. In addition, the SLM-inherited surface defects can cause stress concentration to initiate cracks, reducing the fatigue strength of the printed parts. The review focuses on identifying potential solutions to the surface-finish complex additive manufactured to improve the surface roughness to meet the industry requirements. Therefore, the improvement of the IN718-alloy-parts' surface properties printed by the SLM becomes especially relevant. Currently, different surface post-processing technologies are being developed to obtain the expected surface quality of the SLM-components. As demonstrated, the finish surface enhancement treatments

led to significant improvement in the wear resistance, corrosion resistance, increase in fatigue life, and tensile strength of the metallic materials. Therefore, adapting surface post-processing technologies has become a growing area of interest as an effective tool for improving the functionality and service lifetime of SLM IN718-alloy components. The review aims to analyse the main results of the most systematic studies of the currently developed surface post-treatments aimed to improving the surface-structure quality and properties of the IN718 parts fabricated by SLM. These results contribute to a better understanding of the role of the various-parameters' effects on the surface improvements during the surface post-processing and changes in the structure–phase state, and physical, chemical and mechanical properties. Examples of the effects of a series of surface post-processing methods are presented: laser polishing, mechanical magnetic polishing, cutting finish-machining operations, shot peening, sandblasting technique, ultrasonic-impact treatment, and electrochemical polishing.

Keywords: additive manufacturing, laser melting, Inconel 718 alloy, surface properties, relief, microstructure, hardness.

1. Introduction

Inconel 718 (IN718) was developed in the 1950s with the respective USA patent [1] and is one of the most common industrial heat-resistant alloys of the Inconel family. IN718 is the solid solution or the precipitation-hardened Ni–Fe-based superalloy containing significant amounts of Cr, Nb, and Mo along with lesser amounts of Al and Ti [2–5]. IN718 alloy has attracted increasing attention as an important high-tech metallic material to industries because of its exceptional properties. These include the following: excellent refractory, corrosion and wear resistance characteristics at both elevated and low temperatures; zero expansion coefficient in the temperature range of 0–100 °C; sufficient resistance to the action of chlorine, fluorine, and solutions containing ions of these elements; better resistance to progressive oxidation up to 1100 °C and in the oxidizing-sulphide atmosphere up to 850 °C as they are not vulnerable to vapour, ammonia or sulphur contained gas; with excellent creep properties; oxidation resistance; good tensile strength, fatigue strength, and rupture strength; weldability with outstanding high strengths at elevated temperatures. Summarizing these properties, the IN718 alloy is widely used for the manufacturing of aircraft- and gas-turbine engines, parts for aerospace, nuclear industries, space vehicles, chemical and petrochemical industries, heat exchangers, and other specialized applications requiring heat and/or corrosion resistance [5–11].

In the traditional technology, the IN718 alloy products are manufactured through casting, forging, and heat treatment. As is well known today, the mechanical characteristics of such products significantly depend on their structural and phase state which is quite complex [12–14]. In its wrought form, IN718 ordinarily exhibits several intermetallic phases [15, 16]. The f.c.c. γ-phase forms the material matrix when Ni combines with other constituent elements such as Co, Fe, Cr, Mo, V, and W. The γ''-phase

(Ni$_3$Nb) having the b.c.t. ($D0_{22}$) crystal structure is formed due to the presence of Nb as the principal strengthening element. The secondary strengthening elements are Al and Ti, which cause the development of the ordered f.c.c. γ′-phase (Ni$_3$Al or Ni$_3$Ti). Above 650 °C coarsening of the metastable γ″-phase takes place, which results in the transformation of the γ″-phase into the orthorhombic δ-phase with the composition Ni$_3$Nb. Such a phase is incoherent with the material matrix and causes a reduction in the strength and creep life. In addition, it has been observed that the Laves phases are irregularly shaped phases which form due to Nb segregation with the other alloying elements and having the typical composition of (Ni, Fe, Cr)$_2$(Mo, Nb, Ti), instead of γ′-Ni$_3$Nb. This phase is detrimental to mechanical properties but it can be dissolved in the matrix by proper heat treatments. The content of Ti affects the precipitation of the carbide (TiC) which influences the properties IN718. It has been observed that an increase in TiC content caused finer grain size along with increased hardness. As an example, Table 1 shows the effect of heat treatment and the corresponding phase composition on the tensile properties IN718 [16].

The IN718 alloy is mainly used in the wrought, which is a process that mechanically works a cast billet or ingot several times at a high temperature to receive the final product [17−20]. It is noted that the wrought microstructure is generally more homogeneous and has finer grains than cast microstructure. To obtain the required mechanical properties, a special heat treatment is needed. An example of such processing is given in Table 1.

At present, AM (additive manufacturing) is becoming increasingly popular for a variety of applications, particularly in the fields of the aerospace, energy, automotive and medical industries, due to its capabilities of manufacturing objects that are either prohibitively costly or impossible to manufacture by the traditional processes [21−25]. Among the advantages of AM is producing without additional equipment, including tools, gauges or fixtures, this tool-free production approach can provide flexibility in design, personal customization, high precision in complex

Table 1. **Heat treatment, phases and tensile properties IN718 [15]. Here, S.A., and WQ denotes solution annealing and water quenching, respectively. Std. — heat treatment widely known as 'Standard heat treatment', which is done to get optimum mechanical properties, US — ultimate strength, UTS — ultimate tensile strength, UEL — ultimate elongation**

Heat Treatment / Phases	US, MPa	UTS, MPa	E, GPa	UEL, %
S.A.−650 °C/75 h−620 °C/8 h/WQ/γ + γ′	820	1155	192	28.2
S.A.−750 °C/75 h−620 °C/8 h/WQ/γ + γ″	840	1230	187	20.0
S.A.−800 °C/75 h−620 °C/8 h/WQ/γ + γ′ + δ	720	1190	212	25.5
S.A.−900 °C/75 h/WQ/δ	450	895	148	33.2
Std. S.A.−720 °C/8 h−620 °C/8 h/WQ/γ + γ″	1030	1300	200	21.6

parts, reduced energy and material use, and shortened time for implementation. In addition, manufacturing components have no geometric limitations. Metal AM technology is the process of joining materials layer by layer to produce parts based on the predesigned three-dimensional model data, which is distinguished from traditional subtractive machining techniques. The following most important types of AM can be distinguished for metal printing, namely, selective laser sintering (SLS), selective laser melting (SLM), and electron-beam melting (EBM).

In addition, each AM print technology and material can add further complexity to these objectives. Current technologies for AM printing metal applications include powder bed systems such as DMLS (direct metal laser sintering), EBM (electron-beam melting), and SLM (selective laser melting), or powder feed systems such as LC (laser cladding), LMD (laser metal deposition) and DED (directed energy deposition). Across each of these technologies, some of the most popular alloys being additively manufactured today include titanium, aluminium, stainless steel (304, 316), AlSi10Mg, Ti6Al4V, nickel superalloys (*i.e.*, Inconel 718, Haynes 282, Hastelloy), CoCr, and carbon steel.

Among the additive manufacturing technologies, selective laser melting is finding increasing use in many engineering fields due to its benefits such as short time to market, reduced material waste, possibility to obtain complex and intricate geometries, versatility, ability to produce functionalized parts with unique design and intrinsic engineered features. As is known, it is difficult to produce the IN718 parts using conventional machining methods at room temperature due to excessive tool wear and low material removal rates. In addition, there are the applied IN718 components with very complex in shape with mazy inner chambers or overhangs and that is why it is difficult to manufacture these by the single conventional technology. Therefore, the application of modern non-traditional processing is necessary for the net shape production of In718 parts with complex configurations, high performance and low cost. SLM is one of the actively developed additive technologies for manufacturing parts from In718, one important material for aerospace technology. Therefore, SLM nowadays has a high potential technology and attracted tremendous attention from both manufacturing industries and research institutes/universities.

SLM is the AM procedure that allows the direct printing of the metal component using the computer-aided design (CAD) by fusing fine metal powder in the layers by the high-power laser beam quickly and precisely (Fig. 1). Metal powders used in printing need to be spherical and have the stringent particle size distribution to achieve good packing behaviour. The powders for the next layer are covered on the melted layer, and the laser is again scanned according to the next sliced data providing the layer-by-layer manufacturing on the base plate. This sequence continues until the near-net-shape of the products is formed automatically. SLM can fully
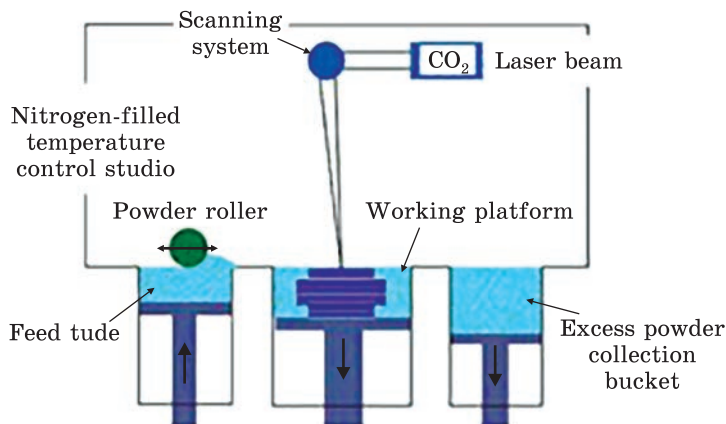
Fig. 1. SLM process schematic view [25]

melt the metal powder into solid printed parts. The main controllers in SLM are the process parameters, which include, *e.g.*, laser power, scan speed, hatch spacing, and scan strategy, which will consequently produce specific microstructure and part properties. An SLM allows producing parts from In718 alloy, which has a dense structure, but it is usually required to carry out the subsequent post-heat treatment or the hot isostatic pressed (HIP) to produce high-quality parts with predictable sufficient mechanical properties such as; density, surface roughness, residual stresses (RS), tensile strength, *etc.*

To achieve the optimal conditions for the desired properties of SLM printed In718, the initial microstructure of the as-printed parts need to be modified by post-processing heat treatments like the following: 'solution treatment followed by ageing' and 'hot isostatic pressing treatment followed by ageing'. The post-processing heat treatment is required to homogenize the bulk material, remove stress and eliminate the microstructure/mechanical property gradient. On the other hand, the poor surface finish of AM parts, however, significantly deteriorates their wear, corrosion and fatigue resistance performance. Numerous works in recent years have shown the critical role of the surface post-treatments on AM materials to obtain controlled, regular and repeatable surface morphology. Therefore, a variety of effective surface post-treatments have been developed and tailored to improve the surface quality and enhance the performance of SLM metal parts. In particular, this is very important for many aerospace applications.

However, it should be noted that the SLM process still faces the apparent limitation in the relationship of the IN718 fabricated parts surface quality, if compared to some alternative metal conventional subtractive manufacturing techniques such as machining. In particular, the fabricated metal parts suffer from excessive residual porosity, and residual tensile stress in the near-surface layer, and the relatively rough surface is formed. The SLM inherited surface defects can cause stress concentration

to initiate cracks, reducing the fatigue strength of the parts. In addition, surface morphology is an important feature of products, from micro- to macro-scale, for several application aspects such as suitability of wettability, adhesion properties, tribological properties, lamination, corrosion resistance, and topological integrity. Consequently, due to the poor surface quality, the SLM fabricated internal surfaces cannot meet the specifications for some real industry applications [27–31]. Therefore, the improvement of the IN718 metal parts surface properties printed by the SLM becomes especially relevant. Currently, different surface post-processing technologies are being developed to obtain the expected surface quality of the SLM components [32–37].

Generally, for the different AM parts, the surface post-processing methods are selected based on the application requirements, geometry complexity, size of the parts and required surface quality. In addition, the combination of different post-methods can be applied. Recently, various methods of surface post-processing methods (finishing) and hardening, such as shot peening, sandblasting, ultrasonic peening or ultrasonic nanocrystal-surface modification, laser shock peening, cavitation peening, barrel finishing, vibratory finishing, machining, electrochemical and laser polishing were studied to enhance the surface properties in the AM printed parts. As demonstrated, these surface enhancement treatments significantly improve the wear resistance, corrosion resistance, fatigue life, the tensile strength of the different metallic materials. Therefore, adapting surface post-processing technologies has become a growing area of interest as an effective tool for improving the functionality and service lifetime of SLM IN718 parts.

The present paper reviews the current development of surface post-treatments aimed at improving the surface quality and structures IN718 parts fabricated by SLM to allow a better understanding of the role of the various parameters' effects on surface improvements during post-processing operation.

2. Laser Polishing

As is well known, laser energy finds application in many sectors of engineering, and polishing is not the exception. Laser polishing (LP) is the potential post-processing used to reduce the surface roughness of the parts manufactured by different conventional techniques. At present, LP drew the researcher's attention to employ it for metallic AM-printed components due to its flexibility, contact-free, eco-friendly and complete automation of this process. The first investigation of LP on AM build Inconel alloy was done in Ref. [38]. In this process, the laser irradiates the metal top surface by low laser pulses with the power density able to cause local surface re-melting of the order of a few nanometres up to micrometres. In
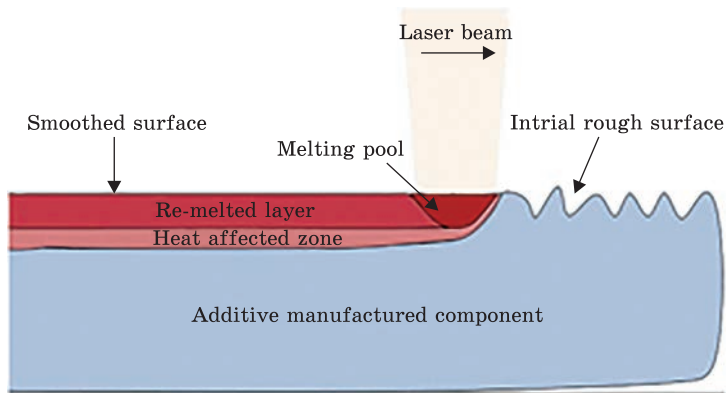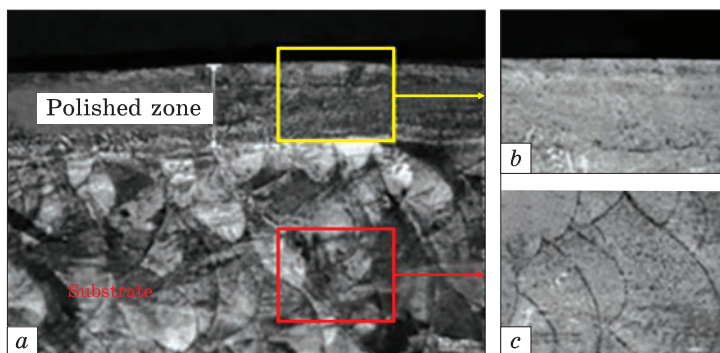
Fig. 2. Schematic of LP [39]

Fig. 3. The OM images of the polished layer cross-section [39]

such a molten pool, the liquid metal of the peak and valley redistributes to the same horizontal level because of the surface tension and gravity. Then, the rapid solidification of the metal molten pool leads to the surface roughness reducing when the laser exposure stops. At last, the height difference of peak-to-valley on the original surface is significantly reduced. Compared with manual polishing, mechanical polishing and chemical–mechanical polishing, LP is a highly efficient, highly flexible, and highly automated processing method. In recent years, LP has been used for metallic materials, especially for difficult machining metals such as IN718 alloy [39]. Figure 2 shows the LP process of SLM IN718 components.

The purpose of the authors [39] was to study the effects of LP on the rough surface and Vickers hardness of SLM IN718 parts. It used the nanosecond pulsed fibre laser (wavelength: $\lambda = 1060$ nm; average output power $P = 100$ W; repetition frequency $f = 1{-}1000$ kHz; pulse duration $t = 12{-}500$ ns; spot diameter of 50 μm). LP takes place in the closed cham-

Table 2. Surface roughness *Ra* and *Rz* of the SLM samples before and after LP [39]

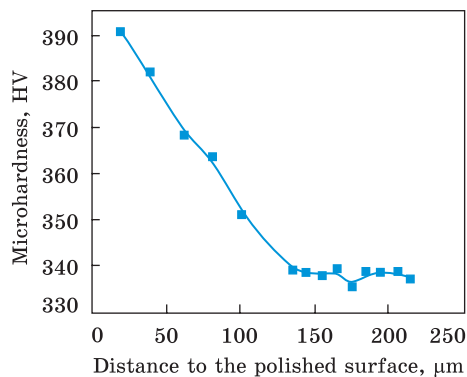| Specimen	*Ra*, μm	*Rz*, μm
As-received	7.5 ± 0.5	31 ± 5
LP	≤0.1	0.6 ± 0.1

Fig. 4. Microhardness distributions in the cross-section of the polished sample [40]

ber, which is filled with inert gas (Ar) to void unwanted oxidations of the surface layers.

The average surface roughness *Ra* and *Rz* before and after LP are listed in Table 2. It can be seen that the SLM samples were effectively polished, and the *Ra* and *Rz* approximately decreased from 7.5 µm to less than 0.1µm, from 31 µm to 0.6 µm, respectively. The optical microscopy (OM) images of the cross-section microstructure after LP are shown in Fig. 2. The thickness of the laser re-melting layer is about 120 µm (Fig. 3, *a*). After LP, the microstructure with higher magnification reveals distinctive segregation patterns generated by the layer scanning paths (Fig. 3, *c*). The indications caused by laser scanning during SLM were eliminated (Fig. 3, *b*).

The microhardness depth distributions are shown in Fig. 4. The average hardness of the bulk sample is about 345 *HV*. After LP, the hardness of the polished surface increases by 27.5% (to about 440 *HV*) than that of the as-received alloy. It was proposed that the precipitation strengthening of γ''- to γ-matrix is the main contribution of polished IN718 samples to their high surface hardness along with the grain refinement caused by laser rapid heating and cooling improved the observed hardness behaviour [41].

Paper [42] showed a significant reduction in the porosity of the SLM samples by LP. The as-printed surface was polished using these nanoseconds pulsed fibre laser modes: wavelength 1.064 nm, pulse duration 150 ns, repetition rate 300 kHz, scanning speed 230 mm/s, overlapping ratio 40%, and spot size 50 µm to polish the specimens under argon-gas protection.

The surface topographies of the as-received and laser-polished samples are shown in Fig. 5. The as-received surface was well polished, and
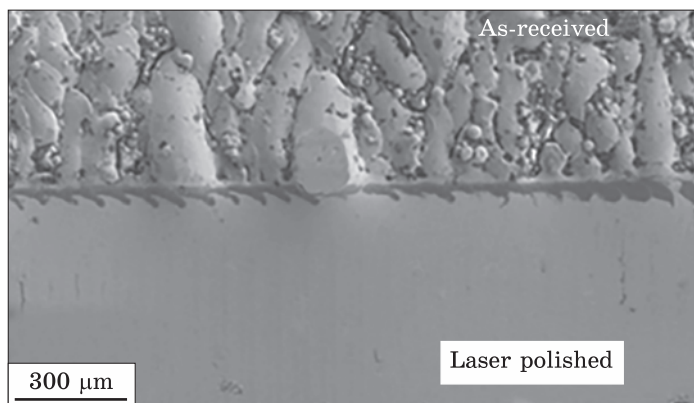

Fig. 5. SEM morphology of the as-received and laser-polished surface [41]

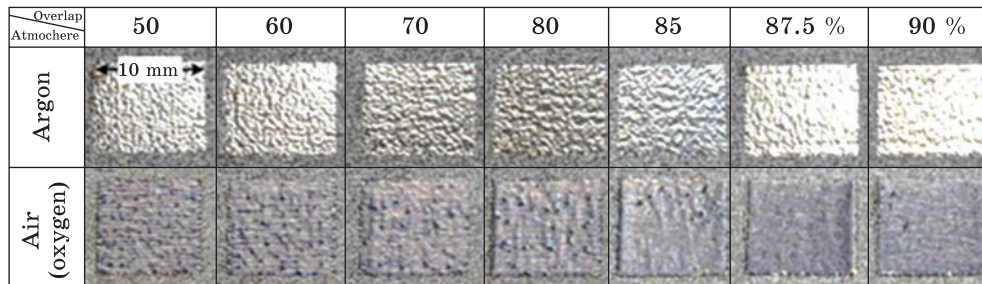| Overlap Atmochere	50	60	70	80	85	87.5 %	90 %
Argon							
Air (oxygen)							

Fig. 6. Physical appearance of the laser-polished samples [42]

no obvious defects were found on the polished surface. As indicated, the average roughness decreased from over *Ra* 10 µm to less than 0.1 µm. The significant porosity reduction was observed in the laser-polished layer, where the surface porosity is reduced by 65.7% compared with that of the as-fabricated SLM surface.

Analysis of the microstructure evolution showed the following results. The typical melted tracks and regular spatial columnar microstructures are observed for the as-received samples. The polished surface layer is characterized by equiaxed grain and columnar grain with an average thickness of 115 ± 12.7 µm. Both the as-received and polished states consist of γ-, γ'- and γ''-phases. X-ray diffraction (XRD) reveals that the preferred growth directions are (200) and (220) crystalline plane during the laser polishing process.

The systematic study of the surface relief dependence on laser parameters of LP was carried out in Ref. [43]. The aim was to optimize the laser polishing parameters to reduce the surface roughness of the printed sample. In this work, two laser regimes were studied. The first regime was the pulsed one, which can generate pulses with durations from 6 to 500 ns and peak power of tens of kW, and the second was the continuous wave regime. For the first regime, Table 3 shows the measured roughness *Ra* for the samples' surfaces polished using different process parameters. It can be seen that the speed increase results in the surface roughness improve-

Table 3. **Resulting surface roughness due to the change of the laser parameters [42]**

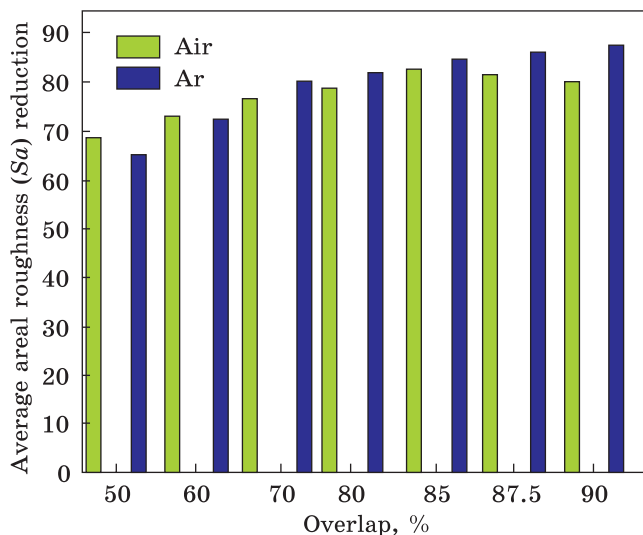| Roughness *Ra*, µm		Speed, mm/s					
		100	200	300	400	500	600
Frequency, kHz	30	1.384	1.083	0.666	0.581	0.526	0.640
	40	1.438	1.257	1.180	1.248	1.080	0.935
	50	1.411	1.446	1.496	1.339	1.352	1.286
	60	1.027	1.462	1.216	1.084	0.887	0.855
	70	1.201	1.254	1.025	0.780	0.759	0.596
	80	0.826	0.999	0.955	0.830	0.734	0.583

Fig. 7. Comparison of the average areal roughness (*Sa*) reduction after applying LP under the effect of the air and argon atmospheres [42]

ment. The initial roughness before LP was *Ra* 1–2 µm. For the LP process parameters of 30 kHz and 500 mm/s, the surface was improved by 56% to *Ra* = 0.5257 µm. It was concluded that the best result was obtained by applying the continuous wave regime by applying parameters of 40 W and a speed of 200 mm/s giving the roughness *Ra* of 0.369 µm and improving the surface roughness by 72%.

The evaluation of the average areal roughness parameters of the SLM samples after LP in the air atmosphere and comparison of the results with those from the inert gas (Ar) chamber setup was carried out [44]. The solid-state Yb: YAG laser with a wavelength of 1030 nm was applied to LP. In this work, seven different overlap values in the range of 50 to 90% were examined for an argon and air atmosphere. The visual images (Fig. 6) observed that the gloss effect was seen for all of the SLM samples that were polished in the argon atmosphere but it is not completely flat. On the other hand, the samples after LP in the air atmosphere become darker due to the formation of the oxidation layers.

At the end of this section, we can sum up (see Fig. 7) that LP allows for the reduction of average roughness by 82.8% and 87.9% for the air and argon atmosphere, respectively.

3. Mechanical Post-Processing Techniques

The effects of the mechanical post-processing magnetic polishing on the surface of the IN718 alloy samples printed by SLM were first studied in Ref. [45]. The magnetic treatment (MT) of the printed specimens was carried out in the conditions of the alternating magnetic field with the use of media: the ferromagnetic needles and the abrasive polishing paste with
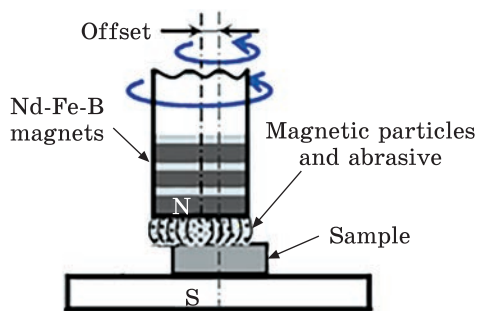
Fig. 8. Schematics of magnetic field-assisted finishing processes [45]

surface-active substances (Fig. 8). Duration of the MT process was 30 min at the ambient temperature. The surface roughness profiles of the as-printed SLM specimens before and after the MT process are shown in Fig. 9.

It was observed that the total height of the roughness profile (Rt parameter) decreased after MT in comparison with that of the as-printed sample. It should also be noted that, after the MT, the peaks of the inequalities are smoothed with an oval/cycle shape due to the plastic deformation of the surface microinequalities by impulse interaction and friction with the media particles. It was also observed that the peaks and valleys' height-parameter magnitudes are smoother in the SLM sample concerning the sampling length. It can be seen that the peak height value of the roughness profile is higher than the valley depth value of the roughness profile in the as-printed sample. The results showed that MT has a large effect on the surface hardness of the samples indicating the potential for the material property improvement in the SLM parts. The MT-processed specimen has a 20% higher hardness (38.8 HRC_{10}) than the as-printed sample (32.2 HRC_{10}).

As the post-processing operation in Ref. [47], the finish machining operations in dry and cold air were performed. The cutting speed and depth of cut were kept constant at 60 m/min and 0.4 mm, respectively; three different feed rate values of 0.08, 0.16, and 0.2 mm/rev were used. Figure 10 shows the measured arithmetic average values of surface roughness of machined SLM samples as the functions of various feed rates under dry and cold air operations. As seen, the average surface roughness (Ra) values of the as-printed samples varied from 19 to 24 μm. After finishing post-treatment, the surface roughness demonstrates substantial reduction when compared with the as-printed state. For all cutting condi-
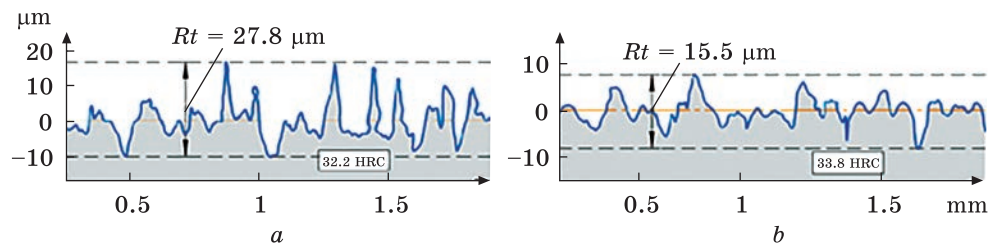

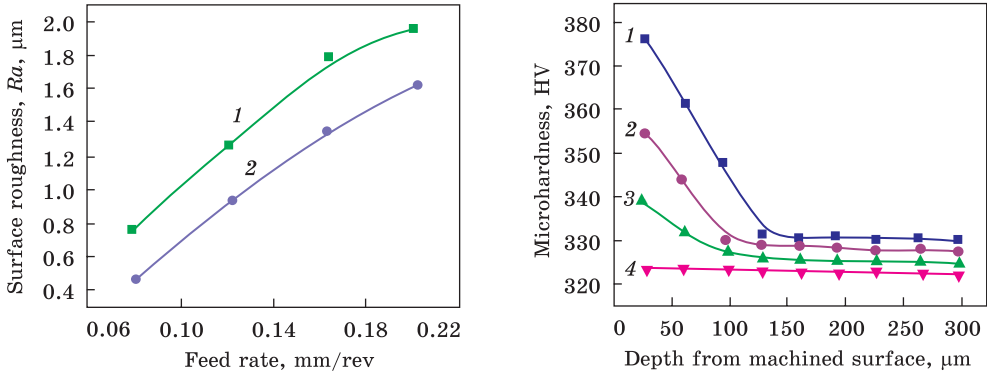*Fig. 9.* Surface roughness profile of SLM (*a*) and MT-processed (*b*) samples [44]

Fig. 10. The surface roughness of the as-printed samples IN718 as the function of the feed rate: *1* — dry; *2* — cold air [46]

Fig. 11. Microhardness of the finish-machined and as-built the SLM IN718 as the feed-rate function (dry): *1* — 0.2; *2* — 0.16; *3* — 0.08; *4* — as-printed, mm/rev [46]

tions and parameters, the largest measured surface roughness value is 1.85 µm. The main conclusion is that the finish machining process resulted in 92% lower when compared to the surface roughness of as-printed samples. As Figure 10 demonstrates, this effect grows as the feed rate decreases.

Figure 11 shows surface and near-surface microhardness distributions after the finish machined under dry conditions at various feed rates and their comparison with as-printed samples (average 322 *HV*). Finish-machining conditions result in increased microhardness on the surface and subsurface. As a result, the larger the feed rate the higher the microhardness level. In addition, the largest microhardness is observed for the sample machined with 0.2 mm/rev feed rate followed by 0.16 and 0.08 mm/rev feed rates. It is more or less similar to the microhardness trend obtained from dry finish machining, as illustrated in Fig. 7. Increased feed rate leads to increased hardness values on the surface and subsurface of finish machined samples. In cold air conditions, the depth of the machining-induced layer is approximately 50 µm that is almost the same as the results obtained from dry machining.

The works [48, 49] were devoted to the effects of the shot peening post-processing as the severe surface plastic deformation on the IN718 surface topography, roughness, waviness, integrity, chemical composition, microstructure, phase state, hardness, and residual stress of the SLM samples. The effects of shot peening, laser shot peening and ultrasonic nanocrystal-surface modification were compared in Ref. [49]. The samples were printed using the following laser parameters: power of 200 W, layer thickness of 60 µm, scanning speed of 700 mm/s, laser spot size of 70 µm, and the distance between scanned lines of 90 µm. As-printed
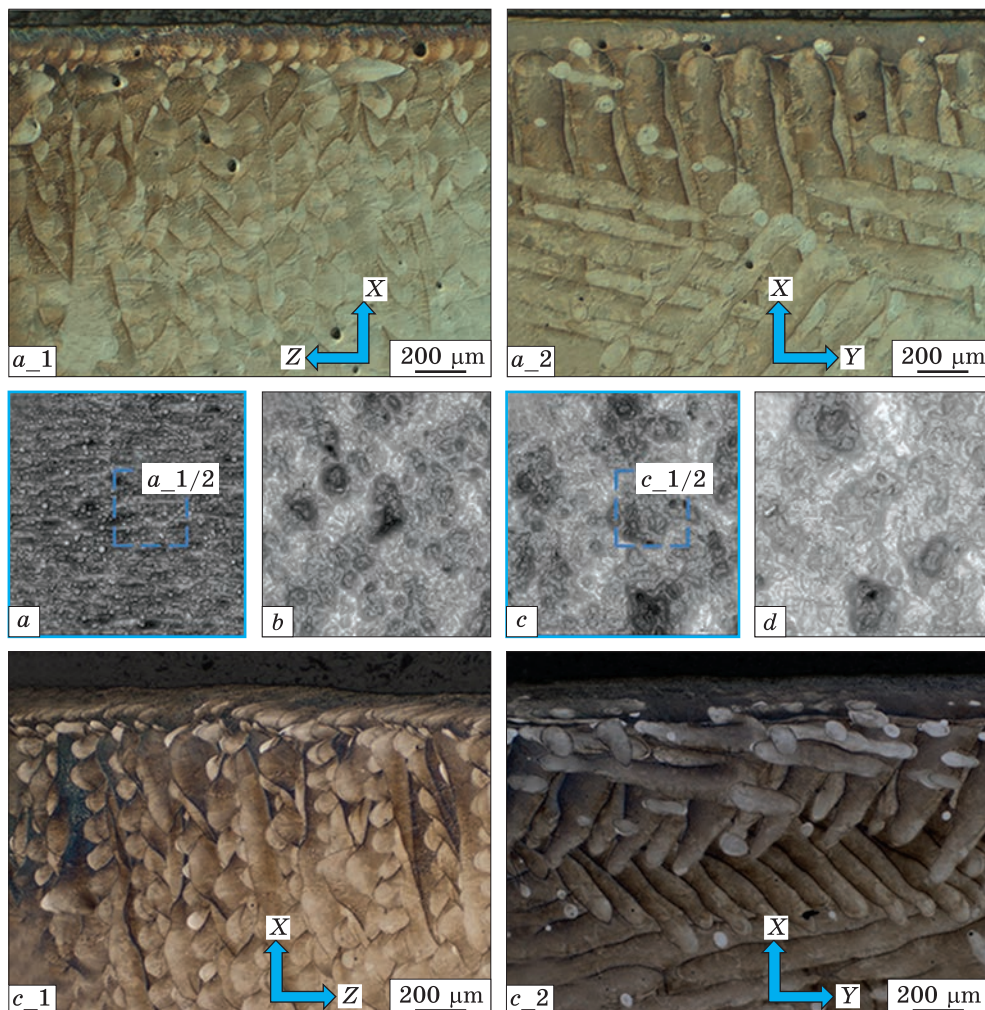
Fig. 12. Surface texture and macrostructure in the near-surface layer of the SLM samples (*a*) and SP1-processed (*b*); SP2-processed (*c*); and SP3-processed (*d*) IN718 specimens: *a*_1 and *a*_2 are the *ZX* and *XY* cross sections of the as-printed sample; *c*_1 and *c*_2 are the *ZX* and *XY* cross sections of SP2-processed specimen [47]

samples were then subjected to the air blast shot peening (SP) using the steel shots (48 HRC) of 0.5 mm in diameter driven perpendicular direction to the specimen surface by the compressed air with different pressure through the nozzle moving transversally to this surface during 60 s. The SP treatment was performed at the peening pressure of 0.4 MPa (SP1), 0.5 MPa (SP2), and 0.6 MPa (SP3), providing full surface coverage.

The surface roughness/waviness of each sample was estimated based on the Ra, Rp, Rv, and Wa. The Rp and Rv parameters are the maximum

Fig. 13. Microhardness distribution in the *ZX* plane (build direction) of the as-printed (*1*) and SP1-processed (*2*); SP2-processed (*3*); and SP3-processed (*4*) of the IN718 samples [47]
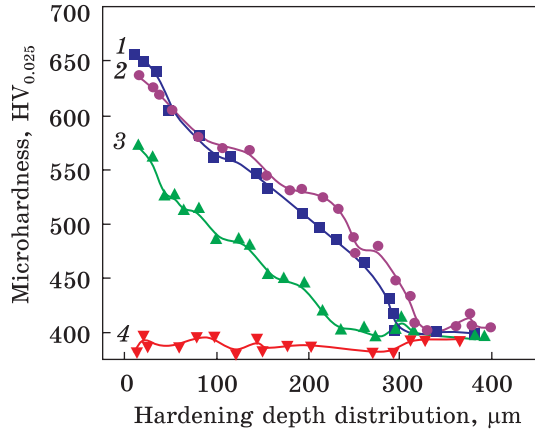
profile peak height and profile valley depth along the sampling length for the roughness profile, respectively. The *Sa* parameter is the arithmetical-mean height of the line to the sample surface, which describes the difference in height of each point compared to the arithmetical mean of the surface. The *Sz* parameter is the maximum profile height of a line to the three-dimensional surface, which is defined as the sum of the largest peak height magnitude and the largest valley depth magnitude within the defined area.

The evolutions of the three-dimensional surface texture after SP performed in different regimes are shown in Fig. 12. As seen, SP led to significant changes in the shape of the roughness and waviness profiles due to the severe plastic deformation providing a new wavy surface microrelief. The arithmetical-mean waviness *Wa* parameter of the profile becomes higher with increasing the magnitude of the air pressure. Unlike the sped samples, the arithmetical-mean height *Sa* parameter of the three-dimensional surface texture/roughness area (*Sa* = 3.79 µm) for the SLM samples has a similar trend to the arithmetical-mean roughness *Ra* parameter of the two-dimensional surface profile. Conversely, to the *Ra* roughness parameters, the *Sa* area-roughness parameters are enlarged after the SP regardless of the processing parameters. However, compared with the maximum height *Sz* of the surface texture for the SLM samples (*Sz* = 47.1 µm), the *Sz* parameter of the SP1- and SP2-processed specimens is decreased by ≈20%, while the SP3 process results in the much higher increase, *i.e.*, the maximum height of the surface texture magnitudes become more than 50% higher (*Sz* = 78.1 µm).

The typical depth distribution of the microhardness after different SP treatments applied is shown in Fig. 13. The surface microhardness (*HV*) measured in the *ZX*-plane correlates well with the surface macrohardness (*HRC*). The SP1 regime led to a ≈60% increase in the near-surface hardness as compared to the untreated SLM samples, while the SP2-induced surface microhardness is approximately 15% higher than that of the SP1-processed specimen. Considering the microhardness distribution in the near-surface layers, one can conclude that the hardening depth is the low-

est ($\approx$220 µm) after the SP1 regime. Moreover, the higher the peening pressure magnitude, the thicker the hardened layer, *i.e.*, $\approx$300 µm and $\approx$330 µm layers were produced after the SP2 and SP3 regimes, respectively.

Compared to the surface roughness of the SLM sample (Ra = 3.77 µm), the Ra roughness parameter of the SP post-processed specimens was, respectively, decreased by $\approx$48, $\approx$53, and $\approx$19% after the SP1, SP2, and SP3 regimes, forming the new wavy microrelief on the surface with reducing the surface defects. At the same time, the Sa area roughness parameter and the arithmetical-mean waviness Wa parameter of the profile were increased after the SP treatment regardless of processing parameters.

As known, the sandblasting technique is often used to make the surface uniform, introduce the residual stresses and thus improve the fatigue performance of the different metallic materials [50, 51]. A combination of the HIP and sandblasting was investigated to reveal the effects on the very high cycle fatigue performance of the SLM IN718 alloy [52]. A series of SiC paper (300−3000 grit) was used to grind the samples, and then the polished samples were chemically etched for 2 min. After the SLM printing, each group of the samples undergoes homogenization (stress relief, 1065 °C/ 1 h), HIP (1160 °C/1500 bar/3.5 h, if necessary), solution (980 °C/1 h) and double ageing (720 °C/8 h, cooling at 50 °C/h until 620 °C and 620 °C/8 h) to eliminate Nb segregation and Laves phase and induce the precipitation strengthening. The parameters of sandblasting process conducted after HIP are summarized in Table 4 for each group of samples.

Since all the investigated samples were homogenization treated, the brittle Laves phases were dissolved at the temperature of homogenization, therefore, no Laves phase is found in both samples. The δ-phase was also dissolved in the homogenization process, but the solution temperature of 980 °C was lower than the precipitation temperature range of the δ phase, so, the δ phase was precipitated at the grain boundary. For the AB state, the δ-phase content is relatively large; the short rod-like and needle-like δ-phases are distributed near the grain boundaries at different angles, and the point-like γ″-phases are distributed inside the grains. The element dis-

Table 4. **The details applied to each group of samples [50]**

Group	Description	Details
AB	AS SLM	Layer thickness: 40 mm; Hatch distance: 110 mm; Laser power: 285 W; Scanning speed: 960 mm/s
SB	Sand-blasted	Pressure: 0.8 MPa; Medium: Grown alumina; Grit: 120; Distance: 100 mm
SBH	Hot Isostatic Pressing (HIP) + Sand-blasting	1160 °C/1500 bar/3.5 h + HIP + Sand-blasting

Fig. 14. Surface morphology of (*a*) AB, (*b*) SB, and (*c*) SBH samples obtained by the SEM [50]
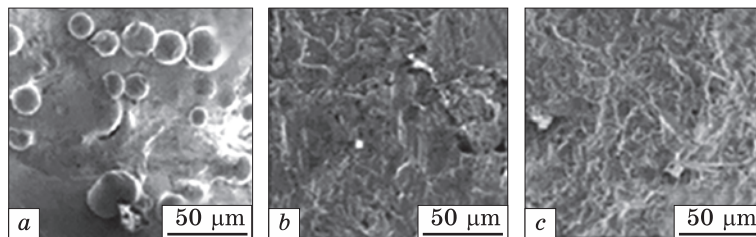
tribution is more homogeneous as the content of the δ-phase precipitated in solution and ageing treatment decreases, and only a small amount of the short rod-like δ-phase can be observed after HIP. In addition, NbC particles, twins, and twin steps can also be formed. The smaller γ'-phase was not found in that study.

The surface morphology of the samples of three groups obtained by the SEM is presented in Fig. 14. As seen the AB sample surface is very uneven, and the peaks and valleys appear alternately. The unmelted powder particles are randomly distributed on the sample surface. For the SB state, the attached powder particles were removed by a high pressure occurred at the grinding by alumina grits, and some scratch marks appeared (Fig. 14, *b*). The surface appears more homogeneous due to deeper surface depressions in the AB samples. For the SBH samples (Fig. 14, *c*), the number of depressions on the surface is larger than that of the SB samples. This is explained by after HIP, the grain size of the alloy increases significantly and the ability to resist plastic deformation decreases. In this investigation, the average Vickers microhardness of the AB, SB, and SBH samples is 496.4, 497.8, and 460.3 *HV*, respectively.

The central area of all samples was selected for the surface height characterization (*Sa*) by the non-contact optical profilometer. It was calculated that the *Sa* for the *AB* sample is of about 4.2 μm. Since the powder particles attached to the surface are removed, sandblasting reduces the arithmetic mean height value to about 3.5 μm. The *Sa* of the SBH surface is higher than that of the SB surface, of about 4.6 μm. During HIP, the wall of the large pores near the surface is collapsed by the pressure, which, in turn, leads to partial depression of the surface. In terms of surface flatness, sandblasting cannot eliminate the adverse effects of HIP in full measure.

The ultrasonic fatigue test including the data plotted as stress *S versus* number *N* (*S*−*N*) of the cycles to failure for three groups of the samples showed the following results. The fatigue resistance of the AB samples is the lowest, and the fatigue strength corresponding to 10^7 cycles is about 207 MPa. The crack nucleation sites of the SB samples are all located on the subsurface and the fatigue strength was greater than that of the AB samples before 10^8 cycles. However, after 10^8 cycles, the fatigue strength decreased to the level of the AB samples. For the SBH samples, the fatigue strength corresponding to 10^7 cycles is significantly improved by about

61.8% compared with the AB samples. The relation σ_f / σ_u for the AB and SB samples are respectively 0.15 and 0.18, which are lower than the SBH samples. The microstructure evolution supposedly comprises the grain size refinement and phase precipitations, which play key roles in the tensile strength. At the same time, the surface state and internal microdefects play a major role in the very high cycle fatigue strength. After HIP and sandblasting, the tested samples failed due to the activation of the slip system induced by the locally higher stress at the triple junctions. Due to the elimination of the defects and the introduction of the surface compressive residual stress, it still shows the best fatigue performance.

3.1. Ultrasonic Impact Treatment

Numerous studies [53–58] have shown that ultrasonic impact treatment (UIT) is one of the ways of severe plastic deformation and an effective technique for fast modification of the surface layers including their structure and complex properties. UIT contributes to the formation of the nanostructured surface layer with improved properties (hardness, tensile strength, wear resistance, fatigue strength, corrosion resistance, biocompatibility, surface roughness) of the different metallic materials. This treatment also significantly reduces the level of residual stresses.

It is well known that the tensile residual stress mostly is induced in the SLM samples. The tensile stresses can be reduced to almost zero value by post-treatment using UIT and the heat treatment helps to homogenize the microstructure [59]. The IN718 samples were printed with the following SLM process parameters: laser power of 90 W; scanning speed of 1200 mm/s; hatch size of 80 μm; powder layer thickness of 25 μm. Since the SLM process usually introduces the residual stresses, post-manufacturing heat treatment is performed to release the induced stresses. In this case, a full annealing treatment is carried out at 955 °C for 1 hour and then the materials are cooled within the furnace. This treatment was done on both the as-printed and heat-treated samples with identical process parameters: static load of 20 N; dynamic load of 20 N; amplitude of 20%; frequency of 20000 strikes/sec; scanning speed of 3000 mm/min; interval of 0.03 mm. In this process, the tungsten carbide ball was attached to the ultrasonic strike device.

Figure 15 shows the image obtained from the optical microscope, taken in a perpendicular (90°) direction to the printing direction. As seen, along the printing direction, columnar grains growth and adjacent layers have same growth direction. After the heat treatment, the homogenous dendritic uniform microstructure is observed.

The residual stresses were measured using the XRD instrument in two orthogonal directions with x-ray diffraction by the $\sin 2\psi$ technique. The results are shown in Fig. 16, where the residual stress curve is for the

Fig. 15. OM microstructure observation under an optical microscope for the as-printed (*a*) and after heat treatment (*b*) IN718 samples [57]
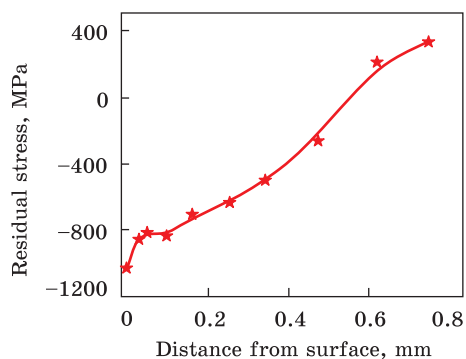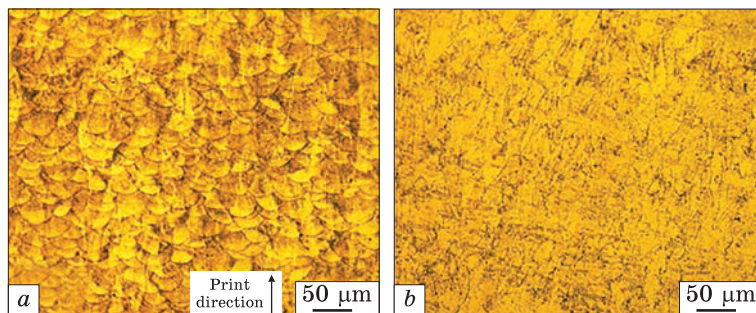

Fig. 16. Residual stress measurement graphs for the samples after Heat + UIT [57]

sample in which UIT treatment was performed on the heat-treated sample. In this case, the surface residual stresses are −655 MPa and −1083 MPa for the 90° printing directions and the depth of compressive residual stresses is around 550 µm.

Effects of the UIT on the surface topography, porosity, hardness and residual stress of the IN718 printed by SLM studied in Refs. [60, 61]. The samples were manufactured using the following SLM parameters: the power of the ytterbium fibre laser of 200 W; scanning speed of 700 mm/s; spot size of 70 µm; stripes spacing of 5 mm; hatch angle of 67°; layer thickness of 60 µm. The UIT equipment contained an ultrasonic generator with a frequency of 21.6 kHz and a power output of 0.8 kW, an acoustic vibration system with a piezoceramic transducer, a step-like horn, and a multi-pin impact head [47−50]. The vibration of the ultrasonic horn causes impact loading. A special impact head is positioned on the horn tip. The high-frequency impacts (1 ± 0.5 kHz) were produced by seven cylindrical pins of 5 mm in diameter positioned in the head forcedly rotated during the treatment (rotation speed of 76 rpm) to provide the lateral component of the load. Pins acquire their kinetic energy from the ultrasonic horn tip and produce impacts by the treated surface providing the normal (vertical) component of the load. The UIT

Table 5. **UIT parameters [60]**

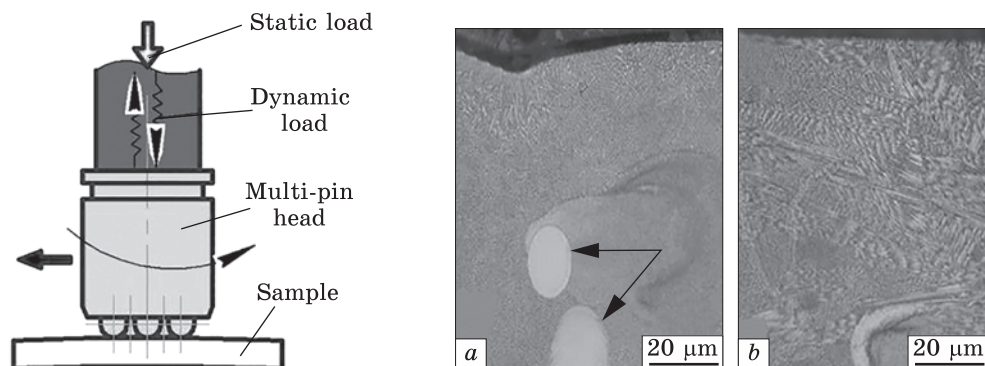| Energy, E, mJ	Quantity of balls/ pins	Impact frequency, f_i, Hz	Treatment time, s	Accumulated energy, ΣE, J/mm^2	Sample thickness, h, mm	Strain, $\varepsilon = \Delta h / h_0$, %	Surface strain, $\varepsilon_s = \Delta h / h_S$, %
2	7	$\approx 1 \cdot 10^3$	120	4.2	3.519	1.074	19.10

Fig. 17. Schemes of the UIT processes [58]

Fig. 18. The surface morphology and images of the near-surface layer of the SLM (*a*) and UIT processed (*b*) IN718 samples [58]

duration was of 120 s, the amplitude of the ultrasonic horn was of ≈18 μm, the static load on the acoustic system was of 50 N, and the specimen feed rate was of 600 mm/min. The scheme and parameters of the UIT process are shown in Fig. 17 and Table 5, respectively. The x-ray diffraction $\sin 2\psi$-based method was used to estimate the residual stress of the SLM and post-processed specimens using a Rigaku Ultima IV diffractometer in a CuK_α-radiation with the graphite monochromator at 30 kV and 30 mA, 2θ (20°−120°) scanning speed of 2°/min. The depth distributions of the residual stress were performed *via* the stepwise electrolytic polishing.

The surface topography of the SLM and post-processed IN718 specimens are compared in Fig. 18. The morphology of the SLM sample side surfaces contains a large number of printing defects (ellipsoidal/spherical balls or shrinkage cavities, partially melted powder particles or spattering powder particles, open pores, and signs of the laser tracks). In addition, the sample surface is rough (*Sz* parameter is ≈60 μm) with irregularities of relatively high height. As seen, the partially melted metal powder or spatters (indicated by arrows in Fig. 18, *a*) are adhered to the surface specimen because of their existence inside the heat-affected zone. Additionally, the unmolten powder particles were found in the near-surface layer (indicated by arrows in Fig. 18, *a*). As a result, the above-mentioned defects essentially deteriorate surface integrity. UIT led to the formation of new surface microreliefs on the post-processed SLM-built samples (Fig. 18, *b*), reducing adverse surface defects. This treatment forms the regular microrelief with a smoother surface (the *Sz* parameter is of ≈20 μm) and lower surface waviness owing to the application of the multipin ultrasonic tool, which produces the sliding impacts of pins by the specimen surface due to forced rotation of the impact head. The registered UIT-caused *Sa* parameter becomes twice lower than that of the SLM-printed samples.
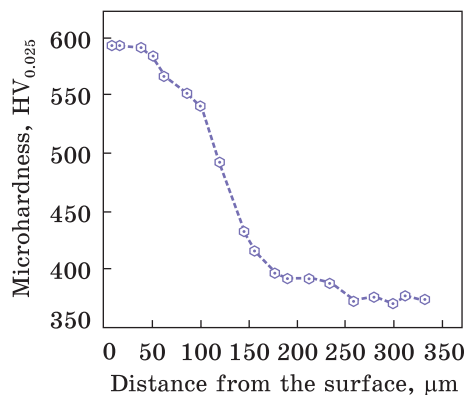
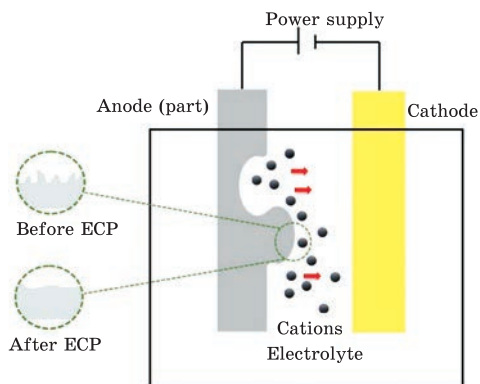*Fig. 19.* Microhardness depth distribution [58]

Fig. 20. Schematic illustration of the ECP cell [60]

Along with the surface microrelief parameters, the residual internal porosity in the near-surface layers is also of special importance for the wear/corrosion and fatigue resistance of the material. Compared to the residual porosity of the SLM sample (0.697%), the porosity magnitudes were respectively decreased by 84% after UIT processes. The UIT process significantly reduced the residual porosity (0.118%) in the near-surface layer.

The near-surface microhardness depth profiles after UIT IN718 are shown in Fig. 19. The UIT process led to a 50% increase in the near-surface hardness, forming the crystallite size of ≈15 µm, as compared to the untreated SLM sample. From the point of view of the desirable prolonged operation life of the SLM-printed parts, the sign and magnitude of the residual stresses are additional critical characteristics. In this study, they were assessed using the x-ray stress analysis. Considering the residual stress magnitudes formed in the subsurface layers of the studied specimens, the tensile residual stresses formed in the SLM sample (120 MPa) because of the large thermal gradients that occurred near the laser spot during rapid heating and cooling of the molten pool were successfully eliminated by post-processing techniques. Moreover, the residual stresses formed by UIT techniques are of compressive character (–428.7 MPa), which correlates well with the data reported in Ref. [61].

3.2. Electrochemical Polishing

Among the available finishing surface treatments, electropolishing (ECP) is an effective and popular process since it can produce a mirror-like surface of the treated material, which however should be conductive. Moreover, it improves the resistance against wear, friction, and corrosion, is efficiently free of stresses or contaminants, and prepares a good base for subsequent coatings. Recent works have shown that ECP is the effective post-surface finishing method for highly complex shaped parts produced
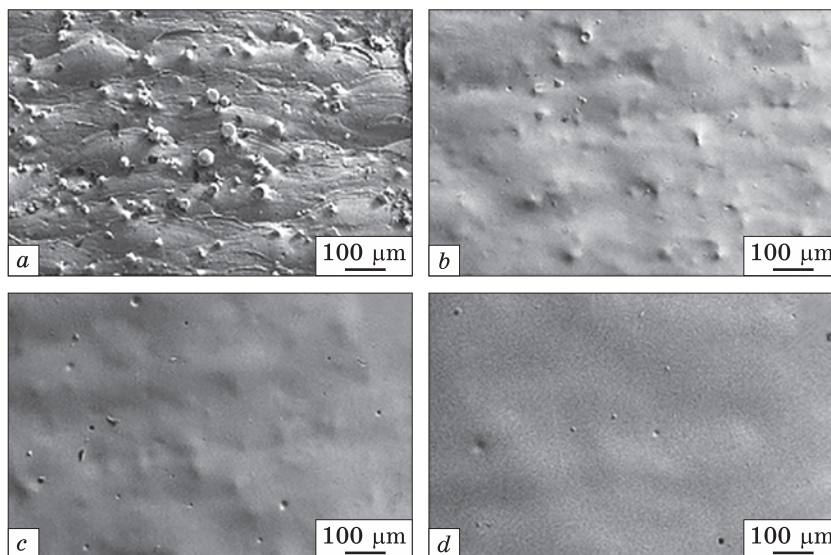
Fig. 21. SEM micrographs showing the surface structures of the as-printed sample (*a*) and samples after ECP for: (*b*) 1 min; (*c*) 4 min; (*d*) 5 min [61]

by AM technology without affecting the bulk properties of the part. ECP is based on the localized anodic low-level electrochemical dissolution process. In other words, the low-temperature ECP is the process that allows removing the micron-sized pieces from the part by immersing it together with electrodes in the electrolyte for the specified time and applying the potential difference of 2 to 20 V DC between the part and electrodes [62]. Acidic electrolytes are generally used as electrolytes for AM metal samples and generally stainless steel, copper, lead, and titanium are used for the electrode. Electrochemically dissolved cations diffuse through the electrolyte to the cathode, where reduction reactions generally yield hydrogen (Fig. 20). Below are the results of the ECP as the post-surface treatment of the SLM IN718 samples.

In Ref. [64], the SLM IN718 samples were manufactured using the following printing parameters: laser power of 350–450 W; scanning speed of 0.3–0.6 m/s, hatch distance of 80 µm; layer thickness of 40 µm; printing temperature of 80 °C; the working chamber was filled with argon gas. The ECP process was carried out at room temperature with a current density of 50 A/dm^2 between the stainless-steel cathode and the sample (anode). The solution used was composed of 20% vol. sulphuric acid in absolute methanol. Figure 21 shows the SEM images of the samples' surface morphology with different ECP durations. As seen, a large amount of the partially melted powder particles are attached to the surface of the as-printed sample (Fig. 21, *a*). It is also obvious that the longer polishing contributes to the improvement in the surface quality significantly. A
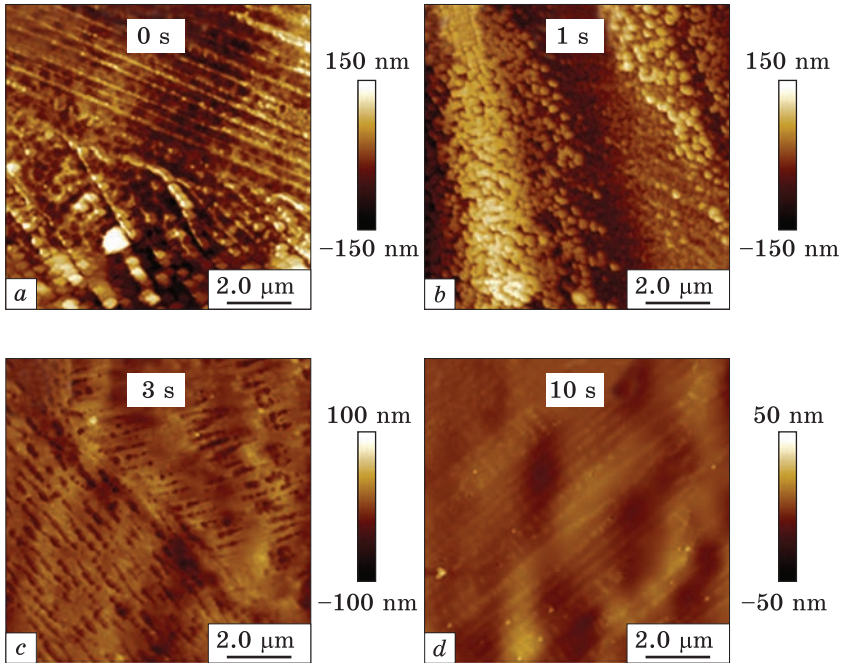
Fig. 22. The atomic force microscopy morphologies of the SLM IN718 samples: as printed (*a*), and polished at 3 A current after: 1 s (*b*), 3 s (*c*), 10 s (*d*) [62]

relatively flat surface with some gaps structure can be found on the sample after ECP with 2 min duration and after 5 min of ECP, the SLM IN718 samples' surfaces are quite smooth and uniform (Fig. 21, *d*). During ECP, the surface roughness was significantly decreased from 6.05 to 3.66 µm.

Nanoindentation testing was carried out to study the mechanical properties of SLM samples after ECP with different durations. It can be observed that the as-printed sample surface has a relatively high nanohardness above 4 GPa. Comparatively, the nanohardness of ECP processed samples ranges from 2.8 GPa to 3.8 GPa with different durations, as shown in Table 6. The reduction of the nanohardness can be attributed to the release of residual stress during the ECP process. The SLM IN718 sample maintained relatively high residual stress because high cooling rate and small laser beam spot. However, the residual stress can be significantly released with material removal during ECP. On the other hand, the γ-precipitates in the as-printed sample surface possess coherent strains and make dislocation hard to move, when compression or tension is applied.

Table 6. **Hardness evolution of the as-printed and after ECP samples with varied polishing durations [61]**

t, s	0	1	2	3	4	5
HV, GPa	4.8	3.8	3.8	3.8	3.5	3.1

According to the authors [64], the existence of δ-precipitate is disadvantageous to the mechanical properties of the alloy. Carbide can only play a key role in grain boundary dislocation, which cannot exhibit the significant capability of surface strengthening on a nanoscale. Thus, the nanohardness value was dropped with the continuous dissolution of γ-precipitates and the appearance of δ-precipitate and carbide during ECP.

In the study [65], the novel and highly efficient isotropic ECP technique for post-surface polishing of the flat and complex SLM IN718 parts was presented. The SLM printing was conducted using the next technical parameters: laser power of 500 W, laser diameter of 100 µm, hatch distance of 110 µm, scanning speed of 300 mm/s, and layer thickness of 40 µm. For isotropic etching of the as-printed samples, the acidic electrolyte comprising commercial-grade H_2SO_4-97% (20 mL) mixed in CH_3OH-99.5% was used. The IN718 samples immersed in the electrolyte were connected to the anode of the DC power supply while the counter electrode (Pt) was connected to the cathode.

Variation in the *Sa* roughness and surface morphologies during the isotropic etching polishing is shown in Fig. 22. The initial 48.9 nm *Sa* roughness of the as-printed sample substrate was raised to 60.8 nm after 1 s etching at the 3 A current in 20 mL H_2SO_4 electrolyte. The initial growth in the *Sa* roughness is due to the formation of the isotropic etching holes. After 3 s etching, the isotropic etching holes merged, and the newly polished surface evolved with *Sa* roughness reduced to 26.3 nm, as shown in Fig. 22, *d*. Therefore, the formation and merging of the etching holes and the evolution of the roughness are due to the generic isotropic etching polishing.

4. Conclusions

IN718 alloy is a heat-resistant, precipitation-hardened alloy that has attracted increasing attention as an important high-tech metallic material to industries because of its exceptional properties, in particular in the aerospace and power generation directions. In the traditional technology, the IN718 alloy parts are manufactured through casting, forging, and heat treatment. However, it is difficult to produce such parts using conventional machining methods at room temperature due to excessive tool wear and low material removal rates. In addition, there is a problem with manufacturing components with very complex shapes with many inner chambers or overhangs.

Currently, additive manufacturing is becoming increasingly effective for a variety of industrial applications due to its capability to manufacture complex components that are either prohibitively costly or impossible to manufacture by traditional technologies. In addition, AM manufacturing of parts has no geometric limitations. Among the additive manufac-

turing technologies, selective laser melting is finding increasing use in many engineering fields due to its benefits such as short manufacturing time, reduced material waste, possibility to obtain complex and intricate geometries, versatility, ability to produce functionalized parts with unique design and intrinsic engineered features. Therefore, the SLM technology nowadays has a high potential and attracted tremendous attention to printing the IN718 parts. However, it should be noted that the SLM fabricated metal parts suffer from the excessive residual porosity and residual tensile stress in the near-surface layer, and the relatively rough surface is formed. The SLM inherited surface defects can cause stress concentration to initiate cracks, reducing the fatigue strength of the parts. Therefore, due to the poor surface quality, the SLM fabricated surfaces cannot meet the specifications for some real industry applications. Therefore, various surface post-processing methods (finishing) are now being developed to obtain the improved surface characteristics of the SLM IN718 components. A large number of publications have demonstrated that these surface enhancement treatments lead to a significant improvement of such properties as wear resistance, corrosion resistance, fatigue life, and tensile strength. Therefore, adapting surface post-processing technologies has become a growing area of interest as an effective tool for improving the functionality and service lifetime of SLM-printed parts.

The analysis of the most systematic studies of the currently developed surface post-treatments aimed at improving the surface structure quality and properties of the IN718 parts fabricated by SLM presented in the review allows a better understanding of the role of the various-parameters' effects on the surface improvements during the surface post-processing operation and changes in the structure-phase state, and physical, chemical and mechanical properties. Examples of the outcomes of the application of the following surface post-processing methods are given: laser polishing, mechanical magnetic polishing, cutting finish-machining operations, shot peening, sandblasting technique, ultrasonic-impact treatment, and electrochemical polishing.

Solution, Dispersion and Work Hardenings, and Surface Finishing' (State Reg. No. 0123U103378) within the NRFU Competition 'Science for the Recovery of Ukraine in the War and Post-War Periods' (application ID 2022.01/0038).

REFERENCES

1. H.L. Eiselstein, *Age-Hardenable Nickel Alloy*, U.S. Patent US3046108A (Published 24 July 1962).
2. H. Qi, *J. Mater. Eng.*, **0**, No. 8: 92–100 (2012);
   https://jme.biam.ac.cn/EN/Y2012/V0/I8/92
3. E. Akca and A. Gürsel, *Periodicals Eng. Nat. Sci.*, **3**: 15 (2015);
   https://doi.org/10.21533/pen.v3i1.43
4. J. Rösler, T. Hentrich, and B. Gehrmann, *Metals*, **9**: 1130 (2019);
   https://doi.org/10.3390/met9101130
5. A. Shard, Deepshikha, V. Gupta, and M.P. Garg, *IOP Conf. Ser.: Mater. Sci. Eng.*, **1033**: 012069 (2021);
   https://doi.org/10.1088/1757-899X/1033/1/012069
6. E.A. Loria, *Superalloy 718: Metallurgy and Applications: Proc. Int. Symp. Metall. Appl. of Superalloy 718* (Minerals, Metals & Materials Society: 1989).
7. E.A. Loria, *JOM*, **44**: 33 (1992);
   https://doi.org/10.1007/BF03222252
8. M.J. Donachie and S.J. Donachie, *Superalloys: A Technical Guide* (ASM International: 2002).
9. S. Sanchez, P. Smith, Z. Xu, G. Gaspard, C.J. Hyde, W.W. Wits, I.A. Ashcroft, H. Chen, and A.T. Clare, *Int. J. Mach. Tools Manuf.*, **165**: 103729 (2021);
   https://doi.org/10.1016/j.ijmachtools.2021.103729
10. S.V. Adzhams'kyy and H.A. Kononenko, *Metallofiz. Noveishie Tekhnol.*, **43**, No. 6: 741 (2021);
    https://doi.org/10.15407/mfint.43.06.0741
11. M. Anderson, R. Patwa, and Y.C. Shin, *Int. J. Machine Tools & Manufact.*, **46**: 1879 (2006);
    https://doi.org/10.1016/j.ijmachtools.2005.11.005
12. Y. Wang, W.Z. Shao, L. Zhen, and X.M. Zhang, *Mater. Sci. Eng. A*, **486**: 321 (2008);
    https://doi.org/10.1016/j.msea.2007.09.008
13. S.C. Medeiros, Y.V.R.K. Prasad, W.G. Frazier, and R. Srinivasan, *Mater. Sci. Eng. A*, **293**: 198 (2000);
    https://doi.org/10.1016/S0921-5093(00)01053-4
14. Y. Wang, W.Z. Shao, L. Zhen, and B.Y. Zhang, *Mater. Sci. Eng. A*, **528**: 3218 (2011);
    https://doi.org/10.1016/j.msea.2011.01.013
15. J.J. Ruan, N. Ueshima, and K. Oikawa, *J. Alloys Compd.*, **737**: 83 (2018);
    https://doi.org/10.1016/j.jallcom.2017.11.327
16. R. Firoz, S.K. Basantia, N. Khutia, H.N. Bar, S. Sivaprasad, and G.V.S. Murthy, *J. Alloys Compd.*, **845**: 156276 (2020);
    https://doi.org/10.1016/j.jallcom.2020.156276
17. E.A. Loria, *JOM*, **40**: 36 (1988);
    https://doi.org/10.1007/BF03258149
18. G. Appa Rao, M. Kumar, M. Srinivas, and D.S. Sarma, *Mater. Sci. Eng. A*, **355**: 114 (2003);
    https://doi.org/10.1016/S0921-5093(03)00079-0

19. R.C. Reed, *The Superalloys: Fundamentals and Applications* (Cambridge: University Press: 2008).

20. T.M. Pollock and S. Tin, *J. Propulsion and Power*, **22**: 361 (2006); https://doi.org/10.2514/1.18239

21. J. Pou, A. Riveiro, and J. Paulo Davim, *Additive Manufacturing* (Elsevier: 2021).

22. I. Gibson, D. Rosen, B. Stucker, and M. Khorasani, *Additive Manufacturing Technologies* (Springer International Publishing: 2021); https://doi.org/10.1007/978-3-030-56127-7

23. P.R. Gradl, C. Protz, O.R. Mireles, and C. Garcia (American Institute of Aeronautics & Ast.: 2022).

24. T. Mukherjee and T. DebRoy, *Theory and Practice of Additive Manufacturing* (Wiley-VCH GmbH: 2023); https://www.wiley.com/en-ae/heory+and+Practice+of+Additive+Manufacturing-p-9781394202270

25. *Additive Manufacturing Technology: Design, Optimization, and Modelling* (Ed. K. Zhou) (Wiley-VCH GmbH: 2023); https://doi.org/10.1002/9783527833931

26. F. Y. Liao, G. Chen, C.X. Gao, and P.Z. Zhu, *Adv. Eng. Mater.*, **4**: 1801013 (2019); https://doi.org/10.1002/adem.201801013

27. C.Y. Yap, C.K. Chua, Z.L. Dong, Z.H. Liu, D.Q. Zhang, L.E. Loh, and S.L. Sing, *Appl. Phys. Rev.*, **2**: 041101 (2015); https://doi.org/10.1063/1.4935926

28. X.Q. Wang, X.B. Gong, and K. Chou, *J. Eng. Manufacture*, **231**: 1890 (2017); https://doi.org/10.1177/0954405415619883

29. X. Peng, L.B. Kong, J.Y.H. Fuh, and H.A. Wang, *J. Manuf. Mater. Process.*, **5**: 38 (2021); https://doi.org/10.3390/jmmp5020038

30. V. Monfared, S. Ramakrishna, N. Nasajpour-Esfahani, D. Toghraie, M. Hekmatifar, and S. Rahmati, *Met. Mater. Int.*, **29**: 3442 (2023); https://doi.org/10.1007/s12540-023-01467-x

31. H.B. Liu, W.H. Cheng, Y.M. Sun, R. Ma, Y.J. Wang, J. Bai, L.N. Xue, X.G. Song, and C.W. Tan, *Coatings*, **13**: 189 (2023); https://doi.org/10.3390/coatings13010189

32. J.-Y. Lee, A. Prasanth Nagalingam, and S.H. Yeo, *Virt. Phys. Prototyp.*, **16**: 68 (2021); https://doi.org/10.1080/17452759.2020.1830346

33. A. Barari, H.A. Kishawy, F. Kaji, and M.A. Elbestawi, *Int. J. Adv. Manuf. Technol.*, **89**: 1969 (2017); https://doi.org/10.1007/s00170-016-9215-y

34. D.A. Lesyk, B.N. Mordyuk, S. Martinez, V.V. Dzhemelinskyi, D. Grzesiak, D. Grochała, and A. Lamikiz, *Lasers Manufact. Mater. Proc.*, **10**: 702 (2023); https://doi.org/10.1007/s40516-023-00231-8

35. A. Malakizadi, D. Mallipeddi, S. Dadbakhsh, R. M'Saoubi, and P. Krajnik, *Int. J. Machine Tools & Manufact.*, **179**: 103908 (2022); https://doi.org/10.1016/j.ijmachtools.2022.103908

36. A. Amanov, R. Karimbaev, C. Li, and M. Abdel Wahab, *Surf. Coat. Technol.*, **454**: 3442 (2023); https://doi.org/10.1016/j.surfcoat.2022.129175

37. M. Kuntoğlu, E. Salur, E. Canli, A. Aslan, M.K. Gupta, S. Waqar, G.M. Krolczyk, and J. Xu, *Int. J. Adv. Manuf. Technol.*, **127**: 1103 (2023); https://doi.org/10.1007/s00170-023-11534-7

38. S. Dadbakhsh, L. Hao, and C.Y. Kong, *Virtual Phys. Prototyp.*, **5**: 215 (2010);
    https://doi.org/10.1080/17452759.2010.528180
39. Z.H.Fang, L.B. Lu, L.F. Chen, and Y.C. Guan, *Procedia CIRP*, **71**: 150 (2018);
    https://doi.org/10.1016/j.procir.2018.05.088
40. Y. Tian, W.S. Gora, A.P. Cabo, L.L. Parimi, D.P. Hand, S. Tammas-Williams, and
    P.B. Prangnell, *Add. Manuf.*, **20**: 11 (2018);
    https://doi.org/10.1016/j.addma.2017.12.010
41. S. Raghavan, B.C. Zhang, P. Wang, C.N. Sun, M.L.S.R. Nai, T. Li, and J. Wei,
    Mater. Manuf. Process, **32**: 1588 (2017);
    https://doi.org/10.1080/10426914.2016.1257805
42. Y.H. Li, Z. Zhang, and Y.C. Guan, *Appl. Surf. Sci.*, **511**: 145423 (2020);
    https://doi.org/10.1016/j.apsusc.2020.145423
43. M. Bureљ and M. Zetek, *MM Sci. J.*, **1**: 3873 (2020);
    https://doi.org/10.17973/MMSJ.2020_03_2019141
44. M. Cwikla, R. Dziedzic, and J. Reiner, *Mater.*, **14**: 1479 (2021);
    https://doi.org/10.3390/ma14061479
45. D. Lesyk, V. Dzhemelinskyi, B. Mordyuk, S. Martinez, O. Stamann, and A. Lamikiz,
    *2020 IEEE 10th International Conference Nanomaterials: Applications & Properties
    (NAP) (9–13 November 2020, Sumy, Ukraine)*;
    https://doi.org/10.1109/NAP51477.2020.9309600
46. H. Yamaguchi, O. Fergani, and P.-Y. Wu, *CIRP Annals*, **66**: 305 (2017);
    https://doi.org/10.1016/j.cirp.2017.04.084
47. Y. Kaynak and E. Tascioglu, *Procedia CIRP,* **71**: 500 (2018);
    https://doi.org/10.1016/j.procir.2018.05.013
48. D.A. Lesyk, V.V. Dzhemelinskyi, S. Martinez, B.N. Mordyuk, and A. Lamikiz, *J.
    Mater. Eng. Perform.*, **30**: 6982 (2021);
    https://doi.org/10.1007/s11665-021-06103-6
49. E. Maleki, O. Unal, M. Gugliano, and S. Bagherifard, *Mater. Sci. Eng. A*, **810**:
    141029 (2021);
    https://doi.org/10.1016/j.msea.2021.141029
50. H. Yu, F. Li, Z. Wang, and X. Zeng, *Int. J. Fatigue*, **120**: 175 (2019);
    https://doi.org/10.1016/j.ijfatigue.2018.11.019
51. S. Bagherifard, N. Beretta, S. Monti, M. Riccio, M. Bandini, and M. Guagliano,
    Mater. Des., **145**: 28 (2018);
    https://doi.org/10.1016/j.matdes.2018.02.055
52. C.L. Yu, Z.Y. Huang, Z. Zhang, J. Wang, J.B. Shen, and Z.P. Xu, *J. Mater. Res.
    Technol.*, **18**: 29 (2022);
    https://doi.org/10.1016/j.jmrt.2022.02.077
53. B.N. Mordyuk, G.I. Prokopenko, M.A. Vasylyev, and M.O. Iefimov, *Mater. Sci.
    Eng. A*, **458**: 253 (2007);
    https://doi.org/10.1016/j.msea.2006.12.049
54. Yu.N. Petrov, G.I. Prokopenko, B.N. Mordyuk, M.A. Vasylyev, S.M. Voloshko,
    V.S. Skorodzievski, and V.S. Filatova, *Mater. Sci. Eng. C*, **58**: 1024 (2016);
    https://doi.org/10.1016/j.msec.2015.09.004
55. M.A. Vasylyev, B.N. Mordyuk, S.I. Sidorenko, S.M. Voloshko, and A.P. Burmak,
    Surf. Coat. Technol., **343**: 57 (2018);
    https://doi.org/10.1016/j.surfcoat.2017.11.019
56. M.A. Vasylyev, S.P. Chenakin, and L.F. Yatsenko, *Acta Mater.*, **60**: 6223 (2012);
    https://doi.org/10.1016/j.actamat.2012.08.006
57. S.P. Chenakin, V.S. Filatova, I.N. Makeeva, and M.A. Vasylyev, *Appl. Surf. Sci.*,
    408: 11 (2017);

https://doi.org/10.1016/j.apsusc.2017.03.004

58. A. Amanov, I.-S. Cho, D.-E. Kim, and Y.-S. Puyn, *Surf. Coat. Technol.*, **207**: 135 (2012);
https://doi.org/10.1016/j.surfcoat.2012.06.046

59. S.S. Kuldeep, S. Jing, K. Vasudevan Vijay, and R. Mannava Seetha, *ASME 2017 12ᵗʰ Int. Manufact. Sci. Eng. Conf. (June 4–8, 2017, Los Angeles, California)*, Paper No. MSEC2017-2918, V002T01A013;
https://doi.org/10.1115/MSEC2017-2918

60. D.A. Lesyk, S. Martinez, B.N. Mordyuk, V.V. Dzhemelinskyi, A. Lamikiz, and G.I. Pro-kopenko, *Surf. Coat. Technol.*, **381**: 125136 (2020);
https://doi.org/10.1016/j.surfcoat.2019.125136

61. D.A. Lesyk, S. Martinez, B.N. Mordyuk, O.O. Pedash, V.V. Dzhemelinskyi, and A. Lamikiz, *Additive Manufact. Let.*, **3**, 100063 (2022);
https://doi.org/10.1016/j.addlet.2022.100063

62. N. Sunay, M. Kaya, and Y. Kaynak, *Sigma J. Eng. Nat. Sci.*, **38**: 2027 (2020);
https://eds.yildiz.edu.tr/sigma

63. Z. Chaghazardi and R. Wüthrich, *J. Electrochem. Soc.*, **169**: 043510 (2022);
https://doi.org/10.1149/1945-7111/ac6450

64. B.C. Zhang, X.H. Lee, J.M. Bai, J.F. Guo, P. Wang, C.-N. Sun, M.L. Nai, G.J. Qi, and J. Wei, *Mater. Des.*, **116**: 531 (2017);
https://doi.org/10.1016/j.matdes.2016.11.103

65. K.M. Ajmal, R. Yi, Z.J. Zhan, J.W. Ji, L.F. Zhang, and H. Deng, *J. Mater. Proc. Technol.*, **299**: 117356 (2022);
https://doi.org/10.1016/j.jmatprotec.2021.117356

М.О. Васильєв[1], Б.М. Мордюк[1], С.М. Волошко[2]

[1] Інститут металофізики ім. Г.В. Курдюмова НАН України,
бульв. Академіка Вернадського, 36, 03142 Київ, Україна

[2] Національний технічний університет України
«Київський політехнічний інститут імені Ігоря Сікорського»,
Берестейський просп., 37, 03056 Київ, Україна

ПОВЕРХНЕВЕ ПОСТОБРОБЛЕННЯ СПЛАВУ INCONEL 718,
ВИГОТОВЛЕНОГО ЗА ДОПОМОГОЮ АДИТИВНОГО ВИРОБНИЦТВА:
СЕЛЕКТИВНЕ ЛАЗЕРНЕ ТОПЛЕННЯ

Розглянуто сплав Inconel 718 (IN718), який є суперсплавом на основі нікелю і широко застосовується в промисловості завдяки своїм чудовим механічним власти-востям навіть за підвищених температур через твердорозчинне зміцнення та дис-персійне зміцнення. Однак через надмірний знос інструменту, погану цілісність по-верхні деталі, його високу твердість і низьку теплопровідність виготовлення виро-бів з IN718 за допомогою традиційних методів оброблення істотно ускладнюється. Це є особливо нагальним для виробів складної конструкції. У зв'язку з цим на-ведено обґрунтування широкого використання сучасного адитивного виробниц-тва для виготовлення виробів із IN718. Найпопулярнішим є метод адитивного ви-робництва, заснований на технології селективного лазерного топлення (СЛТ), що уможливлює створення складних геометричних форм із чудовими властивостями матеріалу. Водночас металеві деталі, виготовлені методом СЛТ, мають надмірну залишкову поруватість, залишкове розтягнення у поверхневому шарі й утворення відносно шорстку поверхню. Крім того, успадковані поверхневі дефекти СЛТ мо-

жуть спричинити концентрацію напруження, щоб ініціювати тріщини, знижуючи втомну міцність надрукованих частин. Огляд зосереджено на виявленні потенційних комплексних рішень щодо фінішного оброблення поверхні, використовуваної з метою поліпшення шорсткості поверхні задля дотримання промислових вимог. Тому поліпшення властивостей поверхні деталей зі сплаву IN718, надрукованих за допомогою СЛТ, набуває особливої актуальності. Наразі розробляються різні технології оброблення поверхні для одержання очікуваної якості поверхні компонентів СЛТ. Було продемонстровано, що фінішне оброблення поверхні значно поліпшує зносостійкість, стійкість до корозії, збільшує довговічність, міцність на розрив металевих матеріалів. Отже, адаптація технологій постоброблення поверхні стає все більшою сферою інтересу як ефективний спосіб для поліпшення функціональності та збільшення терміну служби компонентів із СЛТ-друкованого сплаву IN718. Метою огляду є аналіз основних результатів найбільш систематичних поточних досліджень наразі розвиненими методами постоброблення поверхні, спрямованого на поліпшення якості поверхневих структур і властивостей деталей IN718, виготовлених методом СЛТ. Ці результати сприяють кращому розумінню ролі впливу різних параметрів на поліпшення поверхні під час її постоброблення та зміни структурно-фазового стану, фізичних, хімічних і механічних властивостей. Наведено приклади результатів застосування низки методів оброблення поверхні: лазерного полірування, механічного магнітного полірування, різання, дробоструминного оброблення, піскоструминного оброблення, ультразвукового ударного оброблення, електрохімічного полірування.

Ключові слова: адитивне виробництво, лазерне топлення, сплав Інконель 718, властивості поверхні, рельєф, мікроструктура, твердість.